The evaluation of the damping control in DFIG wind turbine based on impedance analysis method

Chuan Xiang[1], Lei Yang[2] and Chang Chang[3]

[1]Electric Power Research Institute, Yunan Power Grid CO., LTD, Kunming, China
[2]Electric Power Research Institute, Yunan Power Grid CO., LTD. Kunming, China
[3]College of Electrical Engineering, Southwest Jiaotong University, Chengdu, China

E-mail: 1091930966@qq.com, 15911577929@139.com, chris_e_mail@163.com

Abstract. In this paper, the impedance analysis method is utilized to evaluate the performance of the damping control designed for doubly fed induction generator (DFIG) wind turbine. Two categories of damping control are compared and assessed, parameter-optimization-based damping and direct-addition-based damping. First, the impedance analytical model of the control methods are deduced. Then, the scanning results of the impedance based on Matlab/Simulink are given. Hence, the analysis by synthesis can be implemented. It can be concluded that the damping section eliminates the peak of impedance amplitude, thus finally the impedance of the DFIG can be reshaped by adjusting the key parameters of the damping control.

1. Introduction

Along the rapid development of renewable resources in traditional power system, the permeability of the power electronic devices also becomes more significant. During recent years, frequency oscillation problems occur on many occasions and lead to some severe accidents as devices burnt, wind turbine blockade. At present, the phenomena have been investigated to some extent and several measures are also proposed to resolve the problems. The results of [1], [2], and [3] indicate that the oscillation has close relation with the negative damp at specific frequency points caused by the mismatch of the parameters between wind turbine control and grid. Hence, different damping methods are put forward to enhance the operation stability. An integrated PSS controller with virtual inertia and damping control is proposed by [4]. In [5], a damping control strategy considering active and the reactive power is designed for permanent magnet synchronous generator (PMSG)-based wind turbines. But the influence of the key parameter is abbreviated. Similar to some other researches, they are based on the parameter optimization of the tracking curve. Relatively, the damping control is implemented by the addition of the damping components, as in [6]. The general emulating inertia control and drop control based on the structure of direct addition are briefly analyzed and compared. But the performance differences between the damping based on parameter optimization and damping based on the direct addition are still unclear.

Considering the impedance analysis method has the advantage that can simplify the modeling process and improve the stability analysis compared to the state space method [7-8]. In this paper, the impedance analysis method based on the harmonic linearization is utilized to evaluate the two categories of the damping control. The impedance analytical model is deduced, and the amplitude-frequency curves and the phase-frequency curves generated by impedance scanning in

Matlab/Simulink are given. After the comprehensive and comparative analysis, the property differences of the two categories of damping control will be concluded, some optimizing proposal will also be presented.

The structure of this paper is as follows. The simplification and construction in the model of the DFIG wind turbine is presented in section 2. Section 3 introduces and compares the damping control based on the addition of damping components and the damping control based on the parameter optimization. In section 4, the detail impedance analytical models of DFIG are deduced. Section 5 shows and compares the simulation results of impedance scanning among the different damping methods. Finally, the conclusions and suggestions are given in section 6.

2. DFIG Wind Turbine and Control

2.1. DFIG Wind Turbine Modeling

The paper focuses on the damping assessment of the DFIG wind turbine. the DFIG wind turbine is modeled by three portions, wind turbine, Asynchronous induction generator, and AC-DC-AC converter. The crowbar circuit and chopper circuit are neglected, and the wind turbine is constructed as a dual mass block model. The structure of the whole DFIG wind turbine is shown in Figure1.

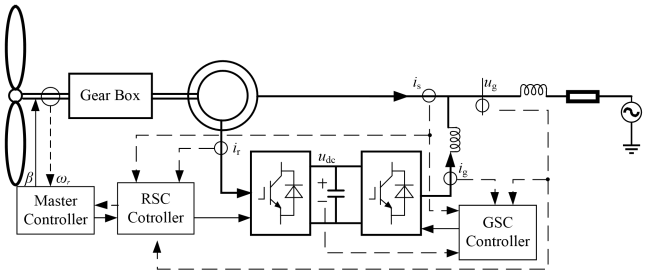

Figure 1. The structure of the DFIG wind turbine.

2.2. Control Structure

The control system is mainly divided into three sections, the master controller, the rotor side converter(RSC) controller and the grid side converter(GSC) controller, as is shown in Fig.1. The master control is adopted to achieve the optimal power calculation and pitch angle adjustment. The structure of the pitch control is shown in Figure 2, and the optimal power calculation is depicted in (1).

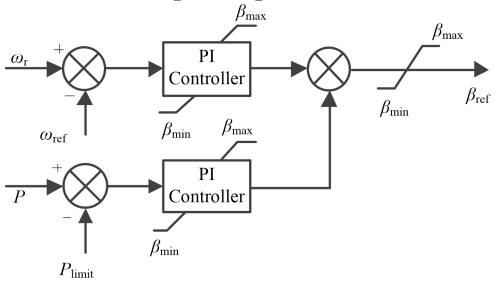

Figure 2. The diagram of the pitch control.

$$P_{out}=\begin{cases} k\omega_r^3, & \omega_0<\omega_r<\omega_1 \\ \dfrac{P_{max}-k\omega_1^3}{\omega_{max}-\omega_1}\left(\omega_r-\omega_{max}\right)+P_{max}, & \omega_1<\omega_r<\omega_{max} \\ P_{max}, & \omega_r>\omega_{max} \end{cases} \tag{1}$$

where k denotes the coefficient of the tracking curve, ω_r is the rotating speed, ω_0 is the accessing speed, ω_1 is the value of the constant speed period, ω_{max} is the limit speed, and the P_{max} denotes the limit of the output power.

The structure of the RSC controller is dual-closed loop, the outer power loop and the inner current loop in d-q frame, as shown in Figure 3.

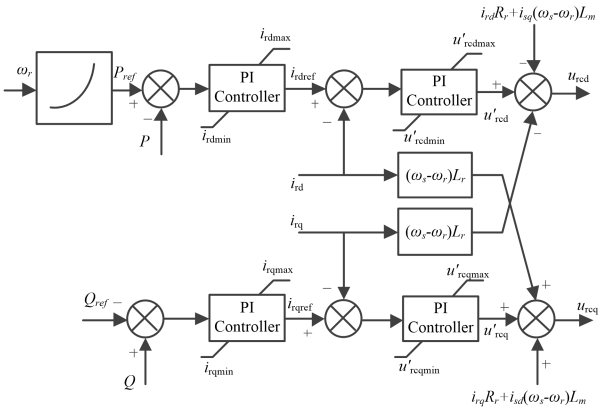

Figure 3. The diagram of the RSC controller.

The GSC controller is also dual-closed loop with the inner current loop in d-q frame, but the outer loop in d axis is the direct voltage control. as depicted in Figure 4.

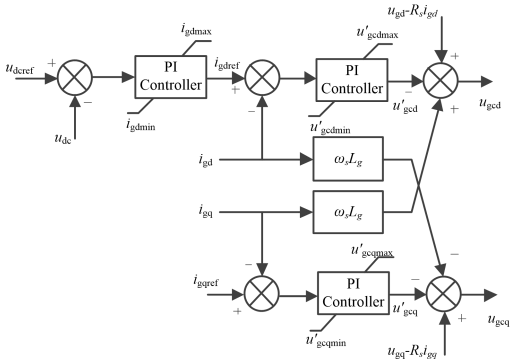

Figure 4. The diagram of the GSC controller.

3. Damping Control

For DFIG wind turbines, since the performance of maximum wind energy capture and the decoupling of the rotating speed and grid frequency, the change of grid frequency will not be responded. Hence the DFIG wind turbines are incapable of inertia response and primary frequency regulation. To make the wind farm participate in the frequency regulation in the power system, the control improvements must be implemented. Considering the RSC has the direct influence on DFIG, the effects will be more remarkable if the work is conducted in the RSC controller, hence the researches of the damping control are generally focus on RSC controller. The studies mainly divided into two sections, the damping controls on the outer loop and the inner loop.

3.1. Damping Control Based on the Optimization

On the active power loop, the improvement can be conducted to fast release or store rotational kinetic energy according to the frequency mutation. Hence the inertia can be stimulated to damp the frequency mutation. The damping based on the tracking curve optimization is depicted in Figure 5, and the optimizing formula is shown in (2).

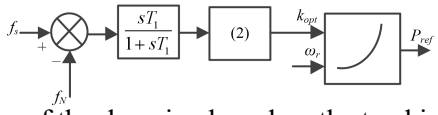

Figure 5. The diagram of the damping based on the tracking curve optimization.

$$k_{opt} = \frac{\omega_{r0}^3}{[\omega_{r0} + 2\pi k_f (f_s - f_N)]^3} k \tag{2}$$

where k_f denotes the coefficient of frequency difference, f_s is the grid frequency, f_N is the nominal frequency, and ω_{r0} denotes the initial rotative speed.

3.2. Damping Control Based on the Optimization

There is another way to achieve the damping on the active power loop, it is the direct adding of frequency difference, as shown in Fig.6. There is no need to acquire the maximum power tracking curve, for most cases, the information is unknown for users.

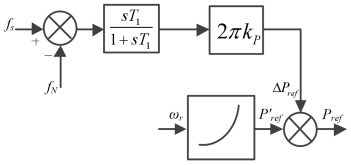

Figure 6. The diagram of the damping based on the direct adding.

Furthermore, if there is enough reactive power margin when the DFIG wind turbine is in operation. The damping effect will be enhanced by dynamically regulating the reactive power. the damping on the reactive power loop is also based on the direct addition of damping components.The structure of the damping on the outer reactive power loop is shown as Fig.7. When the grid voltage difference is below the threshold and the grid frequency difference is beyond the threshold, the function is put into use.

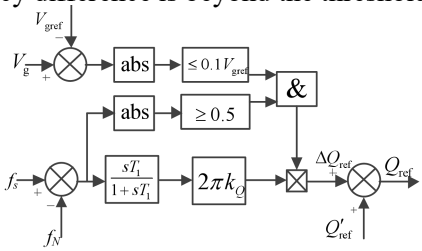

Figure 7. The diagram of the damping on the reactive power loop.

4. Impedance analytical models

Assuming that the capacity of the DC capacitor between the RSC and the GSC is large enough, the voltage can be regarded as a constant value. Hence the DFIG impedance model can be decoupled into two portions， the RSC with induction generator and the GSC, and are defined as Z_1 and Z_2 respectively. The impedance model of DFIG can be depicted by the parallel of Z_1 and Z_2, as shown in (3).

$$Z_{DFIG}=Z_1 // Z_2 = \frac{Z_1 Z_2}{Z_1 + Z_2} \tag{3}$$

4.1. The model of the RSC with induction generator

For the induction generator, in frequency domain, the phasor representation of the stator-side equivalent circuit is shown in Figure 8, and the stator voltage equation is depicted as (4).

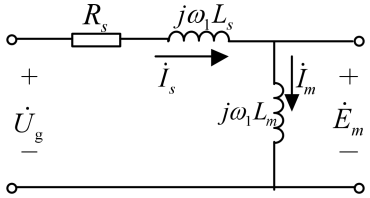

Figure 8. Stator-side equivalent circuit of the induction generator.

$$\begin{cases} \dot{U}_g = \dot{I}_s (R_s + j\omega_1 L_s) + \dot{E}_m \\ \dot{E}_m = j\omega_1 L_m \dot{I}_m \end{cases} \tag{4}$$

where $\dot{U}_g$ is the grid voltage, R_s and L_s are the leakage resistance and leakage inductance of the stator winding, L_m is the inductance of the rotating magnetic field of the stator winding, $\dot{I}_s$ and $\dot{I}_m$ are the stator winding current and excitation current respectively, $\dot{E}_m$ is the induced electromotive force, ω_1 is the stator angular frequency.

Similarly, The equivalent circuit of the rotor-side is shown in Figure 9, and the stator voltage equation can be depicted as (5).

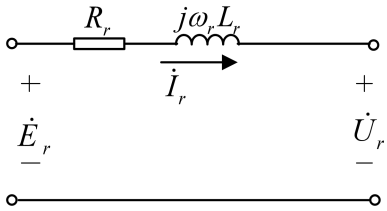

Figure 9. Rotor-side equivalent circuit of the induction generator

$$\dot{E}_r = \dot{I}_r(R_r + j\omega_r L_r) + \dot{U}_r \tag{5}$$

where $\dot{E}_r$ is the induced electromotive force generated by the rotor winding, $\dot{U}_r$ is the rotor voltage, R_r and L_r is the leakage resistance and leakage inductance of the rotor winding, $\dot{I}_r$ is the current of the rotor winding, $\omega_r = \omega_1 - \omega_m$ is the rotor angular frequency, ω_m is the mechanical angular frequency.
Defining slip rate as (6).

$$\sigma_1 = \frac{\omega_1 - \omega_m}{\omega_1} \tag{6}$$

Rotor and stator induced electromotive force ratio can be depicted as (7).

$$\frac{E_r}{E_m} = \frac{4.44\sigma_1 f_1 N_2 k_{w2}\varphi_m}{4.44 f_1 N_1 k_{w1}\varphi_m} = \frac{\sigma_1 f_1 N_2 k_{w2}}{f_1 N_1 k_{w1}} = \sigma_1\alpha \tag{7}$$

where α is the effective turns ratio.
The rotor-side equivalent circuit is converted to the stator side, and the equivalent circuit of induction generator can be acquired and shown in Figure 10.

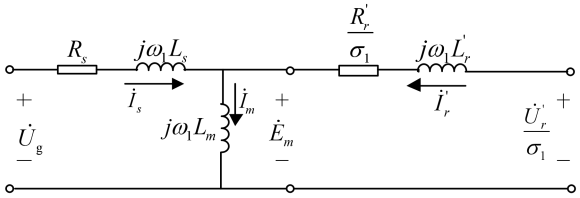

Figure 10. The equivalent impedance circuit of the induction generator.

The parameters on the rotor side is depicted in (8).

$$\begin{cases} \dot{U}_r' = \dfrac{\dot{U}_r}{\alpha}, \dot{I}_r' = -\alpha\dot{I}_r \\ R_r' = \dfrac{R_r}{\alpha^2}, L_r' = \dfrac{L_r}{\alpha^2} \end{cases} \tag{8}$$

As shown in Figure 10, the voltage-current equations of stator side and rotor side can be depicted as (9).

$$\begin{cases} u_{\text{gabc}} = R_s i_{\text{sabc}} + \boldsymbol{L}_{\text{ss}} \dfrac{di_{\text{sabc}}}{dt} + \boldsymbol{L}_{\text{sr}} \dfrac{di_{\text{rabc}}'}{dt} \\ \dfrac{u_{\text{rabc}}'}{\sigma_1} = \dfrac{R_{\text{r}}'}{\sigma_1} i_{\text{rabc}}' + \boldsymbol{L}_{\text{rr}} \dfrac{di_{\text{rabc}}'}{dt} + \boldsymbol{L}_{\text{rs}} \dfrac{di_{\text{sabc}}}{dt} \end{cases} \tag{9}$$

Assuming the system is in symmetrical operation, and the small disturbance signal imposed at the PCC is also symmetric. After the transformation of symmetrical component method, the positive sequence representation of disturbance can be obtained, as shown in (10)

$$\begin{cases} u_{gp} = R_s i_{sp} + (\dfrac{3}{2}L_m + L_s)\dfrac{di_{sp}}{dt} + \dfrac{3}{2}L_m \dfrac{di_{rp}'}{dt} \\ \dfrac{u_{rp}'}{\sigma_p} = \dfrac{R_r'}{\sigma_p} i_{rp}' + (\dfrac{3}{2}L_m + L_r')\dfrac{di_{rp}'}{dt} + \dfrac{3}{2}L_m \dfrac{di_{sp}}{dt} \end{cases} \tag{10}$$

where $\sigma_p = \dfrac{\omega_p - \omega_m}{\omega_p}$.

The voltage and current containing the disturbance can be depicted in phase domain, as shown in (11), (12) and (13).

$$\boldsymbol{U}_g[f] = \begin{cases} \boldsymbol{U}_{s1} = \dfrac{U_{s1}}{2} e^{\pm j\varphi_{s1}}, f = \pm f_1 \\ \boldsymbol{U}_{sp} = \dfrac{U_{sp}}{2} e^{\pm j\varphi_{sp}}, f = \pm f_p \end{cases} \tag{11}$$

$$\boldsymbol{I}_s[f] = \begin{cases} \boldsymbol{I}_{s1} = \dfrac{I_{s1}}{2} e^{\pm j\varphi_{is1}}, f = \pm f_1 \\ \boldsymbol{I}_{sp} = \dfrac{I_{sp}}{2} e^{\pm j\varphi_{isp}}, f = \pm f_p \end{cases} \tag{12}$$

$$\boldsymbol{I}_r[f] = \begin{cases} \boldsymbol{I}_{r1} = \dfrac{I_{r1}}{2} e^{\pm j\varphi_{ir1}}, f = \pm f_1 \\ \boldsymbol{I}_{rp} = \dfrac{I_{rp}}{2} e^{\pm j\varphi_{irp}}, f = \pm f_p \end{cases} \tag{13}$$

The disturbance voltage will result in the disturbance of the phase-locked loop (PLL). The disturbance from the PLL will inject into the system through the d-q transformation of rotor current and d-q inverse transformation of the control voltage. The structure of PLL is shown in Figure 11.

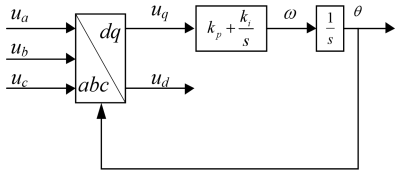

Figure 11. The structure of PLL.

Through the approximating of trigonometric functions, and eliminating the steady state values relationship between practical d-q voltage and ideal d-q-voltage, the PLL output angle can be derived as depicted in (14).

$$\begin{bmatrix} u_{pd}^p \\ u_{pq}^p \end{bmatrix} \approx \begin{bmatrix} u_{pd} + U_q \theta_p \\ -U_d \theta_p + u_{pq} \end{bmatrix} = \begin{bmatrix} u_{pd} \\ -U_{s1} \theta_p + u_{pq} \end{bmatrix} \tag{14}$$

The superscript p means the voltage components in practical conditions, and the subscript p means the components are the disturbances.

The regulator transfer function following the u_q is depicted in (15).

$$H_{pll}(s) = \frac{k_p + \dfrac{k_i}{s}}{s} \tag{15}$$

The overall transfer function can be deduced as (16)

$$F(s) = \frac{jH_{pll}(s)}{1 + U_{s1} H_{pll}(s)} \tag{16}$$

The rotor current in frequency domain and d-q frame can be depicted as (17).

$$\begin{cases} \boldsymbol{I}_{rpd}[f] = \boldsymbol{I}_{rp} \mp j \sin\varphi_{ir1} I_{r1} F(s) \boldsymbol{U}_{sp}, f = \pm(f_p - f_r) \\ \boldsymbol{I}_{rpq}[f] = \boldsymbol{I}_{rp} \pm j \cos\varphi_{ir1} I_{r1} F(s) \boldsymbol{U}_{sp}, f = \pm(f_p - f_r) \end{cases} \tag{17}$$

The output control voltage in d-q frame can be acquired.

$$\begin{cases} \boldsymbol{U}_{rpd}[f] = jI_{r1}F(s)\boldsymbol{U}_{sp}[\sin\varphi_{ir1}H_{ri}(s) - \cos\varphi_{ir1}k_{rd}] \\ \qquad \pm \boldsymbol{I}_{rp}[-H_{ri}(s) \pm jk_r], f = \pm(f_p - f_r) \\ \boldsymbol{U}_{rpq}[f] = jI_{r1}F(s)\boldsymbol{U}_{sp}[\cos\varphi_{ir1}H_{ri}(s) + \sin\varphi_{ir1}k_{rd}] \\ \qquad \mp \boldsymbol{I}_{rp}[\pm \mathrm{j}H_{ri}(s) + k_r], f = \pm(f_p - f_r) \end{cases} \tag{18}$$

where H_{ri} denotes the transfer function of current control of RSC, k_{rd} is the cross coupling coefficient of RSC.

Ignoring the modulation effect of the converter and the delay action of the switch, the control voltage in d-q frame can be transformed to the three-phase coordinate system, then the result can be converted to the stator-side, as shown in (19).

$$\begin{aligned} \boldsymbol{U}'_{rp}[f] = {} & jI'_{r1}F(s \mp j2\pi f_1)\boldsymbol{U}_{sp}H_{ri}(s \mp j2\pi f_1) + \\ & \boldsymbol{I}'_{rp}[-H_{ri}(s \mp j2\pi f_1) \pm jk_{rd}], f = \pm f_p \end{aligned} \tag{19}$$

Combining (10) and (19), The impedance model of the RSC with induction generator can be derived.

$$Z_{1p}(s) = \frac{U_{sp}}{I_{sp}} = \frac{R_s + (\frac{3}{2}L_m + L_s)s - \dfrac{\frac{9}{4}L_m^2 s^2}{\frac{H_{ri}(s \mp j2\pi f_1) \mp jk_r}{\alpha^2\sigma_p} + \frac{R'_r}{\sigma_p} + (L'_r + \frac{3}{2}L_m)s}}{1 - \dfrac{\frac{3}{2}sL_m I'_{r1}F(s \mp j2\pi f_1)H_{ri}(s \mp j2\pi f_1)/\sigma_p}{\frac{H_{ri}(s \mp j2\pi f_1) \mp jk_r}{\alpha^2\sigma_p} + \frac{R'_r}{\sigma_p} + (L'_r + \frac{3}{2}L_m)s}} \tag{20}$$

4.2. The Model of the GSC

Defining $L_a = L_b = L_c = L_g$, the state space equation can be derived.

$$L_g \frac{di_{gabc}}{dt} = u_{gabc} - u_{cabc} \tag{21}$$

where i_{gabc} denote the three phase currents of the GSC, u_{gabc} denote the three phase grid voltages, u_{cabc} denote the three phase output voltages of GSC.

Similar to the section 4.1, the positive sequence representation of disturbance can be obtained, as shown in (22)

$$L_g \frac{di_{gp}}{dt} = u_{gp} - u_{cp} \tag{22}$$

The output control voltage can be deduced.

$$\begin{aligned} \boldsymbol{U}_{cp}[f] = {} & F(s \mp j2\pi f_1)\boldsymbol{U}_{gp}I_{g1}H_{gi}(s \mp j2\pi f_1) + \\ & \boldsymbol{I}_{gp}[-H_{gi}(s \mp j2\pi f_1) \pm jk_g], f = \pm f_p \\ = {} & sL_g\boldsymbol{I}_{gp} + \boldsymbol{U}_{gp} \end{aligned} \tag{23}$$

Hence, the impedance model of the GSC with induction generator can be derived.

$$Z_{2p} = -\frac{\boldsymbol{U}_{gp}}{\boldsymbol{I}_{gp}} = \frac{H_{gi}(s \mp j2\pi f_1) \mp jk_g + sL_g}{1 - F(s \mp j2\pi f_1)I_{g1}H_{gi}(s \mp j2\pi f_1)} \tag{24}$$

When the damping control is utilized in the control system of DFIG, it will reshape the equivalent impedance of the DFIG. Some modification can be implemented in original model to obtain the new impedance model with the damping control. The analysis will benefit from the corresponding impedance model.

5. Simulation and Analysis

In this section, a DFIG detail simulation model is constructed in Matlab/Simulink, and the major electrical parameters and the key control parameters are respectively listed in Table 1 and Table 2. The ω-P curves under different wind speed with β=0 are shown in Figure 12, thus the optimal wind power tracking curve can be acquired. The symmetric voltage disturbances with different frequency and small amplitude are imposed to the steady-state voltage. Then, the current component of corresponding disturbance frequency shall be measured and utilized to calculate the equivalent impedance.

Table 1. Major Electrical Parameters.

Region	Item	Description	Value	Unit
Supply voltage	V_s	Root-mean-square value	575	V
	Fnom	Nominal frequency	50	Hz
Genarator	Pnom	Nominal power	1.5/0.9	MVA
	R_s/ L_s	Stator resistance and inductance	0.023/ 0.18	p.u.
	R_r/ L_r	Rotor resistance and inductance	0.016/ 0.16	p.u.
	L_m	Mutual inductance	2.9	p.u.
	p	Pole-pairs	3	-
Wind turbine	P_{mec}	Nominal mechanical power	1.5	MW
	H_w	Innertial time constant	4.32	-
	D_w	Damping coefficient	1.5	-
	K_w	Elastic coefficient of shafting	1.11	-
GSC inductance	L_g	GSC output inductance	0.3	p.u.

Table 2. Key Control Parameters.

Region	Item	Description	Value
Pitch Control	K_{p_pitch}	Speed loop	1.5
	K_{p_l}/ K_{i_l}	Power limit loop	3/30
RSC control	K_{p_P}/ K_{i_P}	Outer active power loop	0.3/20
	K_{p_Q}/ K_{i_Q}	Outer reactive power loop	0.5/20
	K_{p_ird}/ K_{i_ird}	Inner d-current loop	0.6/8
	K_{p_irq}/ K_{i_irq}	Inner q-current loop	0.6/8
GSC control	K_{p_dc}/ K_{i_dc}	Outer dc voltage loop	8/400
	K_{p_igd}/ K_{i_igd}	Inner d-current loop	0.83/5
	K_{p_igq}/ K_{i_igq}	Inner q-current loop	0.83/5

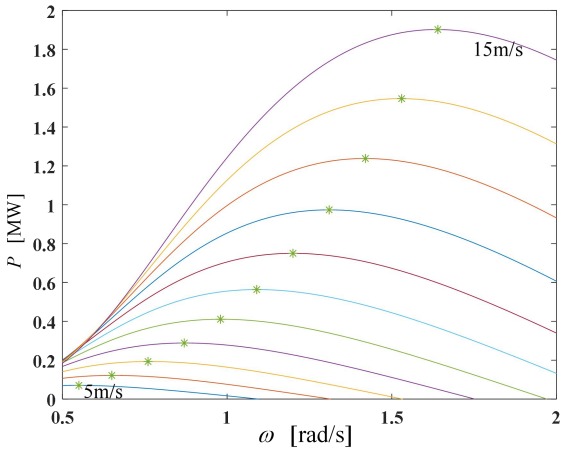

Figure 12. The ω-P curves of the wind turbine.

The impedance scanning results without damping control, with the damping control based on the optimization and the damping control based on addition are implemented, and the corresponding amplitude-frequency curves and phase-frequency curves are acquired, as shown in Figure 13. Here, for the control based on addition, only active power loop is analyzed.

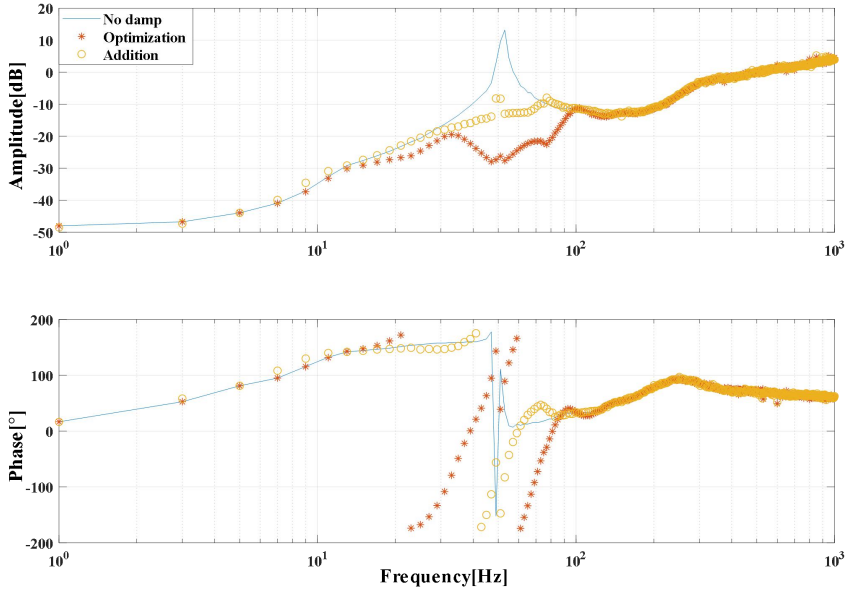

Figure 13. The Bode diagram of the impedance.

It can be seen that in original operation, the amplitude of impedance has a peak. The peak will result in the crossing of the equivalent impedance of DFIG and the impedance of the grid. Generally, the phase of the grid impedance is inductive, if the phase of the DFIG impedance is capacitive, the difference of the DFIG impedance and grid impedance may be greater than 180° . If the situation is at the crossing point, the super-synchronous oscillation or sub-synchronous oscillation may occur.

For the damping based on optimization, it significantly eliminates the peak of impedance amplitude near the nominal frequency point, thus the risk of oscillation can be reduced. It should be noted that there is a big change of the phase, two segments negative phase will prejudice the stability.

For the damping based on direct addition, it also has the capability of reducing the peak. The effect is not as significant as the damping based on optimization, but its negative influence in phase is very small.

The equivalent impedances under different damping coefficients are also obtained to show the influence. The bode diagram of the impedance of damping based on the optimization is shown in Figure 14, and the bode diagram of the impedance of damping based on addition is shown in Figure 15.

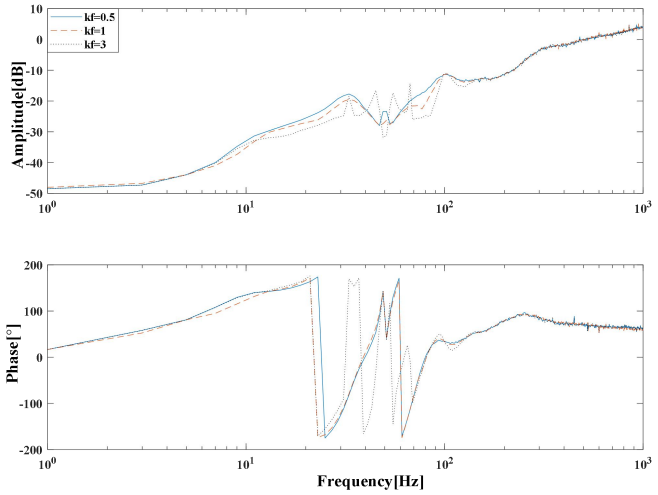

Figure 14. The Bode diagram of the impedance of damping based on the optimization.

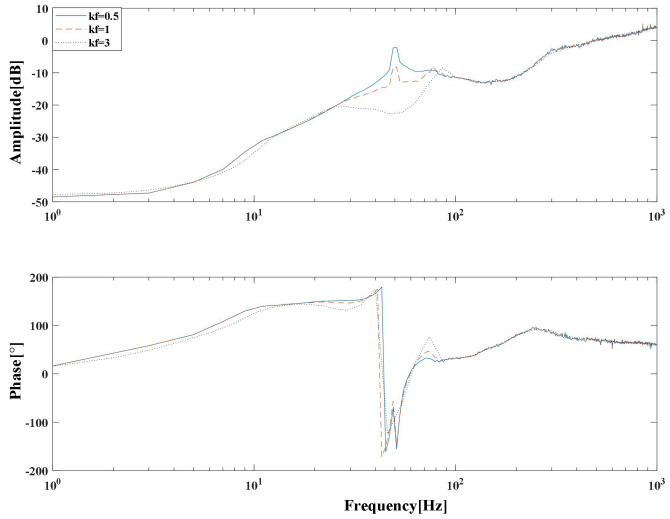

Figure 15. The Bode diagram of the impedance of damping based on addition.

For the change of the damping coefficient k_f in the damping based on the optimization, as shown in Figure 14, it can be seen that from k_f =0.5 to k_f =1,the amplitude of the impedance is further reduced with little change in phase. But when k_f =3, the amplitude has obvious oscillation near the nominal frequency, and three segments of negative phase with large value occurs. Hence the impedance characteristic is deteriorated when k_f =3.

For the change of the k_f in the damping based on addition, as shown in Figure 15, it can be seen that from k_f =0.5 to k_f =3,the amplitude of the impedance is further reduced with little change in phase. The coefficient can be further reduced to get the more suited value.

6. Conclusions

In this paper, the impedance analysis method based on the harmonic linearization is utilized to evaluate the damping based on parameter optimization and the damping based on the direct addition. The impedance analytical model of the DFIG is preliminarily deduced. Based on the simulation model constructed in Matlab/Simulink, the amplitude-frequency curves and the phase-frequency curves generated by impedance scanning are obtained. After the comprehensive and comparative analysis, some conclusion can be acquired.

The amplitude of impedance without the damping has a peak, which will result in the crossing of the equivalent impedance of DFIG and the impedance of the grid. The risk of instability is high.

The damping based on optimization can significantly eliminate the peak of impedance amplitude near the nominal frequency point, thus the risk of oscillation can be reduced. But the big change of the phase results from this method may prejudice the stability.

The damping based on direct addition also has the capability of reducing the peak. Though the effect is not as significant as the damping based on optimization, its negative influence in phase is very small.

For the damping based on optimization, an optimized damping coefficient can be searched in the range from 0.5 to 3. For the damping based on addition, the optimized damping coefficient should be searched over value 3.

In the future work, the analytical impedance considering the damping section will be deduced to further analyze and validate its performance. In addition, the asymmetric condition will be considered in detail by the construction of corresponding positive and negative impedance.

References

[1] Z. Miao, "Impedance-Model-Based SSR Analysis for Type 3 Wind Generator and Series-Compensated Network," in IEEE Transactions on Energy Conversion, vol. 27, no. 4, pp. 984-991, Dec. 2012.

[2] Y. Zhang, Y. Gao, K. Gao, Y. Wang and J. Yang, "Research on Analysis and Suppression Strategy of Subsynchronous Oscillation in Wind Power Grid-Connected System," 2018 Chinese Control And Decision Conference (CCDC), Shenyang, 2018, pp. 4937-4942.

[3] C. Chen, W. Du, H. Wang and T. Littler, "Sub-synchronous oscillations in power systems caused by grid-connected wind farms — A survey of mechanism studies," in CSEE Journal of Power and Energy Systems, vol. 4, no. 4, pp. 495-503, Dec. 2018.

[4] X.Y. Zhang, Y. Fu, Y. Wang, H. Wang and C. Fu,"Integrated PSS Controller of Variable Speed Wind Turbines withVirtual Inertia and Damping Control," Transctions of China Electrotechnical Society, vol.30, no.1 ,pp. 159-169, Jan. 2015.

[5] Y. Wang, X.Y. Zhang, M.H. Li and X.R. Zhu, "Damping Control of PMSG-Based Wind Turbines for Power System Oscillations," Transctions of China Electrotechnical Society, vol.27, no.12 ,pp. 162-171, Dec. 2012.

[6] J.X. Zhao, W. Gao, M.X. Shangguan, X.B. Zha, S. Yue and Y.H. Liu, "Review on frequency regulation technology of power grid by wind farm," Power System Protection and Control, vol.45, no.21, pp. 157-169, Nov. 2017.

[7] Y. Wang, X. Wang, F. Blaabjerg and Z. Chen, "Harmonic Instability Assessment Using State-Space Modeling and Participation Analysis in Inverter-Fed Power Systems," in IEEE Transactions on Industrial Electronics, vol. 64, no. 1, pp. 806-816, Jan. 2017.

[8] J. Sun, "Impedance-Based Stability Criterion for Grid-Connected Inverters," in IEEE Transactions on Power Electronics, vol. 26, no. 11, pp. 3075-3078, Nov. 2011.